TomoGRAF: A Robust and Generalizable Reconstruction Network for Single-View Computed Tomography

Di Xu, Yang Yang, Hengjie Liu, Qihui Lyu, Martina Descovich, Dan Ruan and Ke Sheng*

Please send all correspondence to:

Ke Sheng, Ph.D.
Professor and Vice Chair
Department of Radiation Oncology
University of California, San Francisco
ke.sheng@ucsf.edu

Abstract

Computed tomography (CT) provides high spatial resolution visualization of 3D structures for scientific and clinical applications. Traditional analytical/iterative CT reconstruction algorithms require hundreds of angular data samplings, a condition that may not be met in practice due to physical and mechanical limitations. Sparse view CT reconstruction has been proposed using constrained optimization and machine learning methods with varying success, less so for ultra-sparse view CT reconstruction with one to two views. Neural radiance field (NeRF) is a powerful tool for reconstructing and rendering 3D natural scenes from sparse views, but its direct application to 3D medical image reconstruction has been minimally successful due to the differences between optical and X-ray photon transportation. Here, we develop a novel TomoGRAF framework incorporating the unique X-ray transportation physics to reconstruct high-quality 3D volumes using ultra-sparse projections without prior. TomoGRAF captures the CT imaging geometry, simulates the X-ray casting and tracing process, and penalizes the difference between simulated and ground truth CT sub-volume during training. We evaluated the performance of TomoGRAF on an unseen dataset of distinct imaging characteristics from the training data and demonstrated a vast leap in performance compared with state-of-the-art deep learning and NeRF methods. TomoGRAF provides the first generalizable solution for image-guided radiotherapy and interventional radiology applications, where only one or a few X-ray views are available, but 3D volumetric information is desired.

Introduction

Computed tomography (CT) acquires x-ray projections around the subject to generate 3D cross-sectional images. Compared to 2D radiographs, where the depth information along the ray direction is lost and structures superimposed, CT enables the 3D representation of rich internal information for quantitative structure characterization. Analytically, Tuy's data sufficiency condition covering a sufficient sampling trajectory is required for mathematical rigid reconstruction[1]. Violating Tuy's condition leads to geometry and intensity distortion in the reconstructed images (referred to as limited-angle artifacts in the following). Besides the sampling trajectory, a minimal sampling density is required to avoid streak artifacts that can severely corrupt the image with sparse, e.g., <100 views.

On the other hand, data-sufficient conditions may not always be met due to practical limitations, including imaging dose considerations, limited gantry freedom, and the need for continuous image guidance for radiotherapy and interventional radiology[2,3]. For instance, the total ionizing radiation exposure in mammograms is kept low to protect the sensitive tissue[4]. However, 2D mammograms without depth differentiation can be inadequate with dense breast tissues. Digital breast tomosynthesis (DBT), a limited-angle tomographic breast imaging technique, was introduced to overcome the problem of tissue superposition in 2D mammography while maintaining a low dose level. In DBT, limited projection views are acquired while the X-ray source traverses along a predefined trajectory, typically an arc spanning an angular range of 60° or less. The acquired limited angle samplings are then reconstructed as the volumetric representation with improved depth differentiation but still inferior quality to CT[5,6]. In different applications, the acquisition angles are not restricted, but the density of projection is reduced to lower the imaging dose[7,8] or to capture the dynamic information in retrospectively sorted 4DCT[9,10], resulting in sparse views in each sorting bin.

Image reconstruction from sparse-view and limited-angle samplings is an ill-posed inverse problem. Due to insufficient projection angles, the conventional filtered back-projection (FBP)[11] algorithm, algebraic reconstruction technique (ART)[12], and simultaneous algebraic reconstruction technique (SART)[13] suffer from limited-angle artifacts that worsen with sparser projections. Over the past few decades, substantial effort has been made to advance the development of sparse-view CT from two general avenues. One line of research lies in developing regularized iterative methods based on the compressed sensing (CS) [14] theory. For instance, Sidky et al. proposed the adaptive steepest descent projection onto convex sets (ASD-POCS) method by minimizing the total variation (TV) of the expected CT volume from sparsely sampled views[15]. Following that, the adaptive-weighted TV (awTV) model was introduced by Liu et al. for improved edge preservation with local information constraints[16], while an improved TV-based algorithm named TV-stokes-projection onto Convex sets (TVS-POCS) was proposed immediately after to eliminate the patchy artifacts and preserving more subtle structures[17]. Apart from the TV-based methods, the prior image-constrained CS (PICCS)[18], patch-based nonlocal means (NLM)[19], tight wavelet frames[20], and feature dictionary learning[21] algorithms were introduced to further improve the reconstruction performance in representing patch-wise structure features. More recently, deep learning (DL) techniques were explored for improved CT reconstruction quality in the image or sinogram domain. The image domain methods learn the mapping from the noisy sparse-view reconstructed CT to the corresponding high-quality CT using diverse network structures such as feed-forward network[22,23], U-Net[24], and ResNet[25]. The sinogram domain methods work on improving/mapping the FBP

algorithm[26–29] or interpolating the missing information in the sparse-sampled sinograms[30–33] with DL techniques. These and other deep learning-based sparse view CT reconstruction studies are comprehensively reviewed in Podgorsak et al. and Sun et al. [34,35].

Yet, with the exception where the same patient's different CT was used as the prior[36], little progress was made in reconstructing high-quality tomographic imaging using less than ten projections, a practical problem in real-time radiotherapy or interventional procedures. For the former, an onboard X-ray imager orthogonal to the mega-voltage (MV) therapeutic X-ray provides the most common modality of image-guided radiotherapy (IGRT). However, a trade-off must be made between slow 3D cone beam CT (CBCT) and fast 2D X-rays [37,38]. A similar trade-off exists in interventional radiology[39]. When real-time interventional decisions need to be made in the time frame affording one to two 2D X-rays, yet 3D visualization of the anatomy is desired, a unique class of ultra-sparse view CT reconstruction problems combining extremely limited projection angles *and* sparsity is created.

With the advancement of deep learning and more powerful computation hardware, several recent studies proposed harnessing inversion priors through training data-driven networks for single/dual-view(s) image reconstruction. Specifically, Shen et al. designed a three-stage convolutional neural network (CNN) trained on patient-specific 4DCT to infer CT of a different respiratory phase using a single or two orthogonal view(s)[40]. Ying et al. built a generative adversarial network framework (X2CT-GAN) with a 2D to 3D CNN generator to predict tomographic volume from two orthogonal projections[41]. Though promising, their generalization and robustness to external datasets have not been demonstrated and may be fundamentally limited by two factors: First, they generate volumetric predictions purely from 2D manifold learning. As a result, these networks are incapable of comprehending the 3D world and the projection view formation process[43]. Second, a prerequisite for deep networks with complex enough parameters to implicitly represent 2D to 3D manifold mapping is large and diverse training data, a condition difficult to meet for medical imaging[44].

An effective perspective to mitigate those problems is to leverage intermediate voxel-based representation in combination with differentiable volume rendering for a 3D-aware model, which requires smaller data to generalize. The Neural Radiance Fields (NeRF)[45] model successfully implemented this principle for volumetric scene rendering. NeRF proposed synthesizing novel views of complex scenes by optimizing an underlying continuous volumetric scene function using a sparse set of input views. NeRF achieved this by representing a scene with a fully connected deep network with the input of 5D coordinates representing the spatial location, view direction, and the output of the volume density and view-dependent emitted radiance at the spatial location. The novel view was synthesized by querying 5D coordinates along the camera rays and using volume rendering techniques to project the output color and densities onto an image[45]. NeRF was designed to generate unseen views from the same object and typically required fixed camera positions as supervision. As an improvement, GRAF, a 3D-aware generative model 2D-supervised by unposed image patches, introduced a conditional radiance field generator trained within the Generative Adversarial Network (GAN) framework[46] that is capable of rendering views of novel objects from given sparse projection views[43].

The success of NeRF and GRAF motivated their applications to solve the 3D tomography problems. MedNeRF[42] was proposed by Corona-Figueroa et al. for novel view rendering from a few or single X-ray projections. MedNeRF inherits the general GRAF framework, remains 2D-supervised, and assumes visible-light photon transportation configuration in the generator with an addition of self-supervised loss to the discriminator. However, there are distinct differences between CT volume reconstruction and "natural object" 3D representation rendering in terms of the available choices of training supervision, imaging setup, and properties of the rays. Specifically, 3D training supervision (object mesh with information on surface color) is often hard to acquire for "natural objects." In contrast, existing CT scans are an ideal volumetric training ground truth (GT) for fitting a 3D tomographic representation learning model. Moreover, optical raytracing works by computing a path from an imaginary camera (eye) through each pixel in a virtual screen and calculating the color of the object visible through the virtual screen via simulating ray reflection, shading, or refraction on the object surface (Fig. 1 (b)). The solving target of optical ray tracing is the object surface color (r, g, b) and density σ in a 3D location (x, y, z). Meanwhile, x-rays are transported from the focal spot through an object to the detector plane, accounting for scattering and attenuation (Fig. 1 (c)). The goal of CT reconstruction is voxel-wise material densities δ at a 3D location (x, y, z). Because of these major differences between natural scenes and 3D medical images, the direct application of NeRF has not resulted in usable CT with ultra-sparse views.

To overcome the challenges in ultra-sparse view CT reconstruction while maintaining the superior NeRF 3D structure representation efficiency, we introduced an x-ray-aware tomographic volume generator, termed TomoGRAF, to simulate CT imaging setup and use CT and its projections for 3D- and 2D-supervised training. TomoGRAF is further enhanced with a GAN framework and computationally scaled with sub-volume and image patch GTs training. To the best of our knowledge, this is the first pipeline that informs the NeRF simulator with X-ray physics to achieve generalizable high-performing CT volume reconstruction with ultra-sparse projection representation.
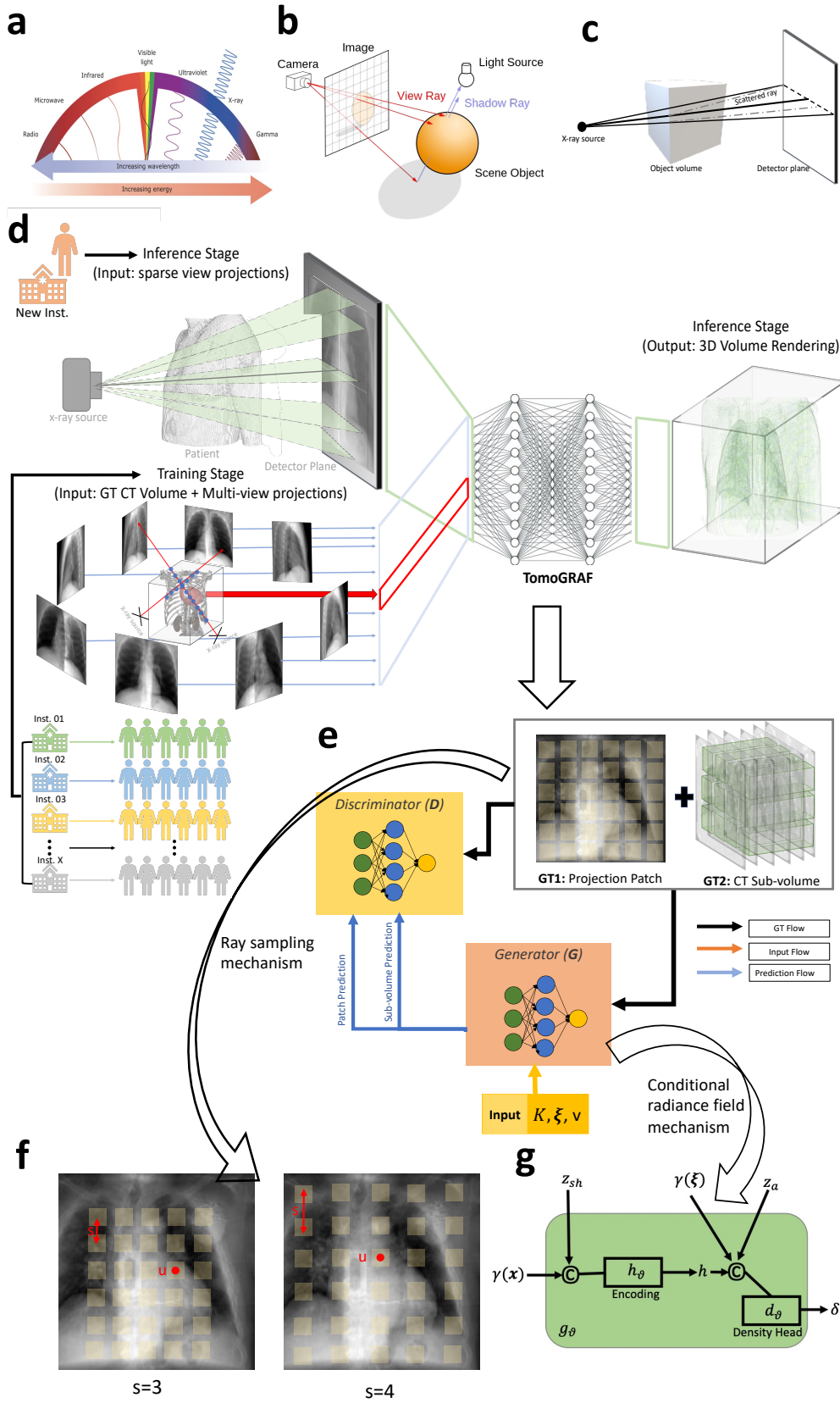
a

Microwave
Radio
Infrared
Visible light
Ultraviolet
X-ray
Gamma

Increasing wavelength
Increasing energy

b

Camera
Image
Light Source
View Ray
Shadow Ray
Scene Object

c

X-ray source
Object volume
Scattered ray
Detector plane

d

New Inst.

Inference Stage
(Input: sparse view projections)

x-ray source
Patient
Detector Plane

Inference Stage
(Output: 3D Volume Rendering)

Training Stage
(Input: GT CT Volume + Multi-view projections)

TomoGRAF

Inst. 01
Inst. 02
Inst. 03
Inst. X

e

Ray sampling mechanism

Discriminator (D)

GT1: Projection Patch **+** **GT2:** CT Sub-volume

Patch Prediction
Sub-volume Prediction

GT Flow
Input Flow
Prediction Flow

Generator (G)

Input K, ξ, v

Conditional radiance field mechanism

f

s=3

s=4

g

z_{sh}

$\frac{z_{sh}}{\gamma(\xi)}$

z_a

$\gamma(\xi)$

z_a

$\gamma(x)$ → Ⓒ → h_ϑ → h → Ⓒ

Encoding

g_ϑ

d_ϑ → δ

Density Head

h → Ⓒ

d_ϑ → δ

Density Head

Figure 1: Architecture of the proposed TomoGRAF framework. a, The illustration of energy/wavelength difference between visible lights and X-rays. **b,** The visualization of object imaging with visible lights in 3D. **c,** The visualization of object imaging with X-ray in 3D. **d,** The visualization of the training and inference stage of TomoGRAF. TomoGRAF references multi-view projections and the corresponding CT volume during training using data collected from multiple institutes (inst.) and will only require sparse-view projections referencing at the inference stage to render the predicted CT volume from a new institute. **e,** The pipeline of the TomoGRAF network. TomoGRAF works on projection patches and CT sub-volume in training. The input to TomoGRAF consists of source setup matrix K, view direction (pose) ξ and 2D sampling pattern v. **f,** The ray sampling mechanism in a patch of the projection input to TomoGRAF. u represents the center of the sampled patch, and s refers to the distance between two sampled patches. **g,** The design of conditional radiance field in TomoGRAF with a fully connected coordinate network (g_ϑ) which consists of shape encoding h_ϑ and density head d_ϑ.

Results

The results of TomoGRAF, MedNeRF, and X2CT-GAN with 1 or 2 views for 2D projection and volume rendering are visually demonstrated in Fig.2 and Fig. 3, with accompanying statistics reported in Tab. 1 and Fig. 4. TomoGRAF consistently outperforms MedNeRF and X2CT-GAN in both tasks with the most evident advantage in 1-view volume reconstruction.

For 2D projection rendering, TomoGRAF achieves marginally better results than MedNeRF. Both models maintain the overall critical body shapes of GT, and TomoGRAF visualizes more detailed morphology, such as heart, spine, and vascular structures. In comparison, the projection results of X2CT-GAN show visible distortion and significantly worse quantitative performance.

For 3D volume reconstruction, as shown in Figure 3, with 1-view, TomoGRAF depicts rich and correct anatomical details with visible tumors and a pacemaker consistent with GT. The results are further refined with the second orthogonal X-ray view, improving fine details' recovery. In comparison, MedNeRF and X2CT-GAN fail to render patient-relevant 3D volumes with 1 or 2 views. MedNeRF loses most anatomical details; X2CT-GAN deforms 3D anatomies that do not reflect patient-specific characteristics, such as lung tumors and the pacemaker.

As shown in Tab. 1, TomoGRAF is vastly superior in quantitative imaging metrics, achieving SSIM and PSNR of 0.79 ± 0.03 and 33.45 ± 0.13, respectively, vs. MedNeRF (SSIM at 0.37 ± 0.05 and PSNR at 7.68 ± 0.10) and X2CT-GAN (SSIM at 0.31 ± 0.012 and PSNR at 14.39 ± 0.19). There is a similar reduction in RMSE. Additionally, we can observe from Fig. 4 that the SSIM distribution of TomoGRAF is highly left skewed and leptokurtic in both 1 and 2-view-based volume rendering, with the majority clustering tightly towards the higher end, while that of MedNeRF and X2CT-GAN tends to be normal and moderately right-skewed (values lean towards the lower end).

Tab. 2 shows the 3D reconstruction performance with or without 3D supervision using 1, 2, 5, and 10 views as input. Using more views improved both volume and projection inference performance. 3D GT training markedly boosted the model performance in 3D volume rendering only. Fig. 5

shows line profile comparisons for varying view inputs. 1 view TomoGRAF recovered major structures but missed fine details, which were better preserved with more X-ray views.
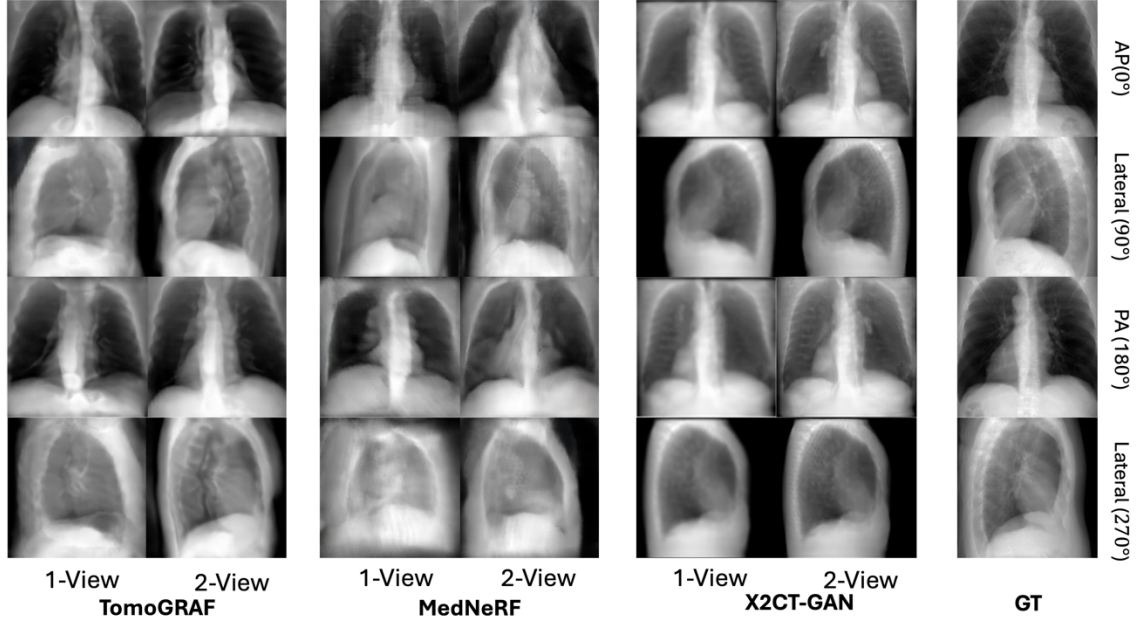

Figure 2: Lung projection rendering in four 360°-clockwise-rotated (visualized every 90° of rotation) views from a patient in a test set. Projections from X2CT-GAN are generated by applying the DRR synthesis algorithm on predicted CT volumes since the original X2CT-GAN was only designed to predict the CT volume. TomoGRAF and MedNeRF directly predicted the 2D projections. Results rendered by referencing 1-view and 2-views are both visualized. All the images are shown with a normalized window of [0, 1].
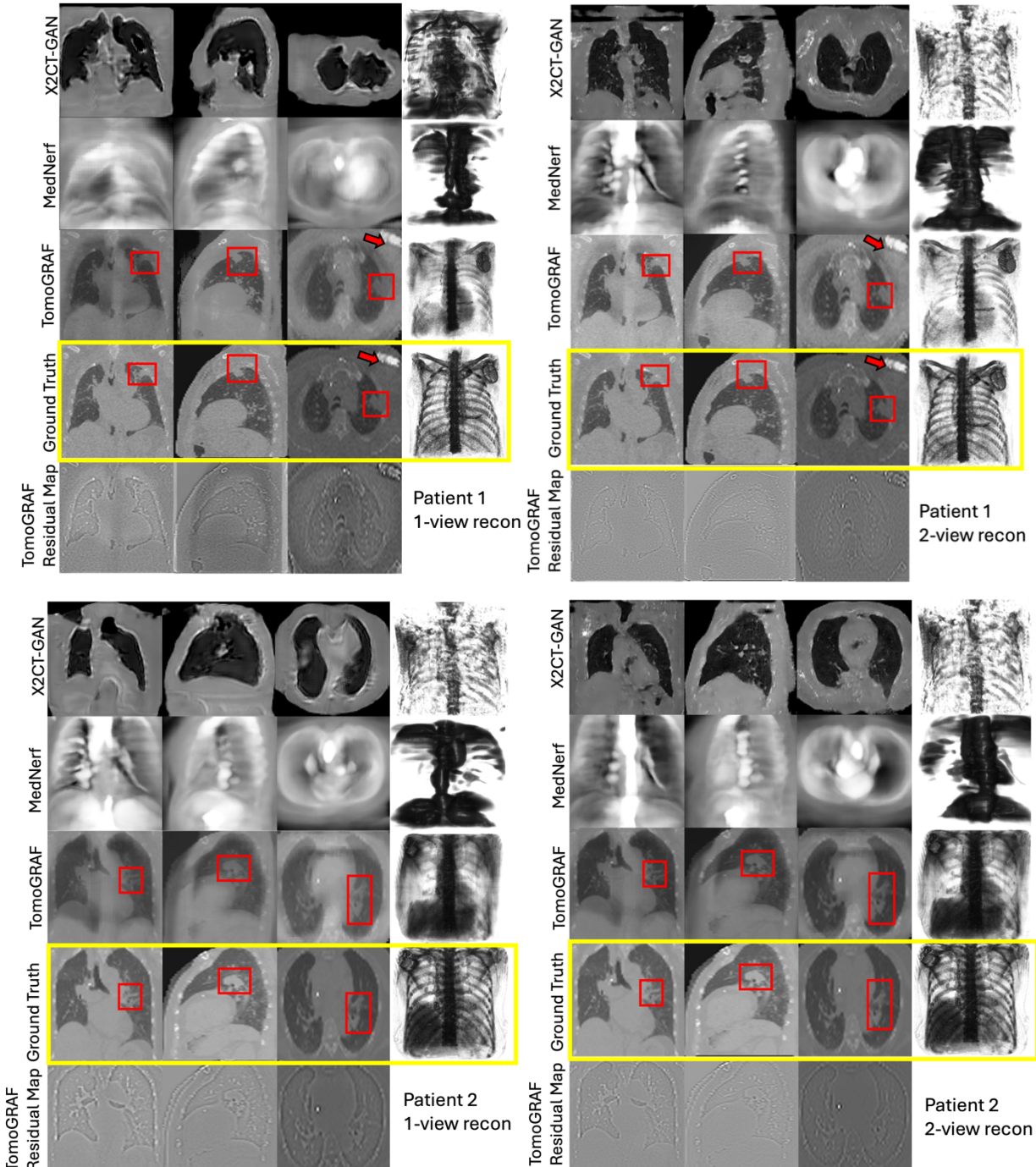
Figure 3: CT Reconstruction results for two representative patients in the test set. Only the residual maps of the TomoGRAF are shown, as the two comparison methods result in a large mismatch with GT. The images are visualized in a lung window with (a Hounsfield Unit width and level) of (1500 -600). The red boxes denote the lung tumors, while the arrows point to the pacemaker in patient 1.
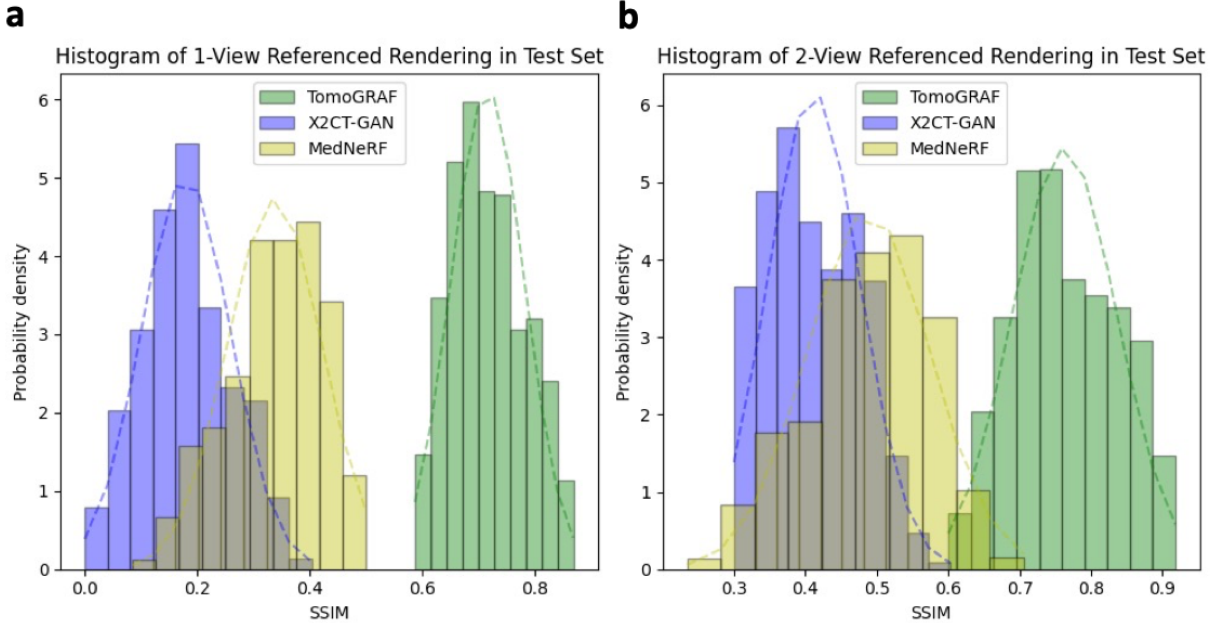
Figure 4: a, Patient-wise evaluated SSIM distribution (visualized using histograms with smoothed trend curves) of 1-view-based volume rendering results of TomoGRAF, X2CT-GAN, and MedNeRF in the test set. **b,** Patient-wise evaluated SSIM distribution (visualized using histograms with smoothed trend curves) of 2-view-based volume rendering results of TomoGRAF, X2CT-GAN, and MedNeRF in the test set.

	Modality	1-View				2-Views			
		SSIM↑	PSNR(dB)↑	RMSE(HU)↓	Inference Time (s)↓	SSIM↑	PSNR(dB)↑	RMSE↓	Inference Time (s)↓
CT Volume	**X2CT-GAN**	0.31 ± 0.12	14.39 ± 0.19	386.69 ± 27.43	<u>0.27</u>	0.48 ± 0.06	17.35 ± 0.21	347.76 ± 25.46	<u>1.31</u>
	MedNeRF	0.37 ± 0.08	7.68 ± 0.10	321.87 ± 22.87	527.78 ± 15.48	0.50 ± 0.09	18.21 ± 0.09	299.49 ± 21.58	865.46 ± 30.81
	TomoGRAF	<u>0.79</u> ± 0.03	<u>33.45</u> ± 0.13	175.48 ± 10.47	344.25 ± 10.32	<u>0.85</u> ± 0.04	<u>35.89</u> ± 0.13	146.73 ± 9.63	719.46 ± 26.78
Projection	**X2CT-GAN**	0.34 ± 0.11	11.88 ± 0.19	51.96 ± 7.98	-	0.51 ± 0.09	18.23 ± 0.26	47.64 ± 7.32	-
	MedNeRF	0.67 ± 0.07	25.02 ± 0.15	36.48 ± 4.36		0.69 ± 0.08	27.31 ± 0.14	33.42 ± 4.01	
	TomoGRAF	<u>0.69</u> ± 0.03	<u>25.43</u> ± 0.14	34.37 ± 4.58		<u>0.71</u> ± 0.04	<u>27.99</u> ± 0.13	31.22 ± 4.12	

Table 1: Statistical results evaluated on the test set. The best results from each metric are underscored. ↑ indicates the higher the statistical value, the better, and vice versa for ↓. SSIM and PSNR are calculated with images normalized to [0,1] scales and RMSE are calculated based on Hounsfield Units (HUs).

	Reference View	3D Supervised Training	SSIM↑	PSNR(dB)↑	RMSE(HU)↓	Inference Time (s)↓
CT Volume	1	Y	0.79 ± 0.03	33.45 ± 0.13	175.48 ± 10.47	344.25 ± 10.32
		N	0.66 ± 0.05	26.76 ± 0.16	197.47 ± 11.24	
	2	Y	0.85 ± 0.04	35.89 ± 0.13	146.73 ± 9.63	719.46 ± 26.78
		N	0.69 ± 0.06	29.87 ± 0.19	168.35 ± 10.21	
	5	Y	0.88 ± 0.03	37.23 ± 0.13	138.45 ± 9.12	987.35 ± 37.89
		N	0.72 ± 0.04	30.15 ± 0.18	147.56 ± 9.79	
	10	Y	0.93 ± 0.01	39.98 ± 0.11	127.68 ± 8.78	1238.81 ± 46.72
		N	0.75 ± 0.01	31.86 ± 0.18	138.98 ± 9.54	

Table 2: Statistical results of TomoGRAF ablation study evaluated on test set. 1/2/5/10-Views represent the number of views used for reconstruction reference. Training with and without 3D

CT supervision is also compared in the current table. ↑ indicates the higher the statistical value, the better, and vice versa for ↓. SSIM and PSNR are calculated with images normalized to [0,1] scales and RMSE are calculated based on Hounsfield units (HUs).
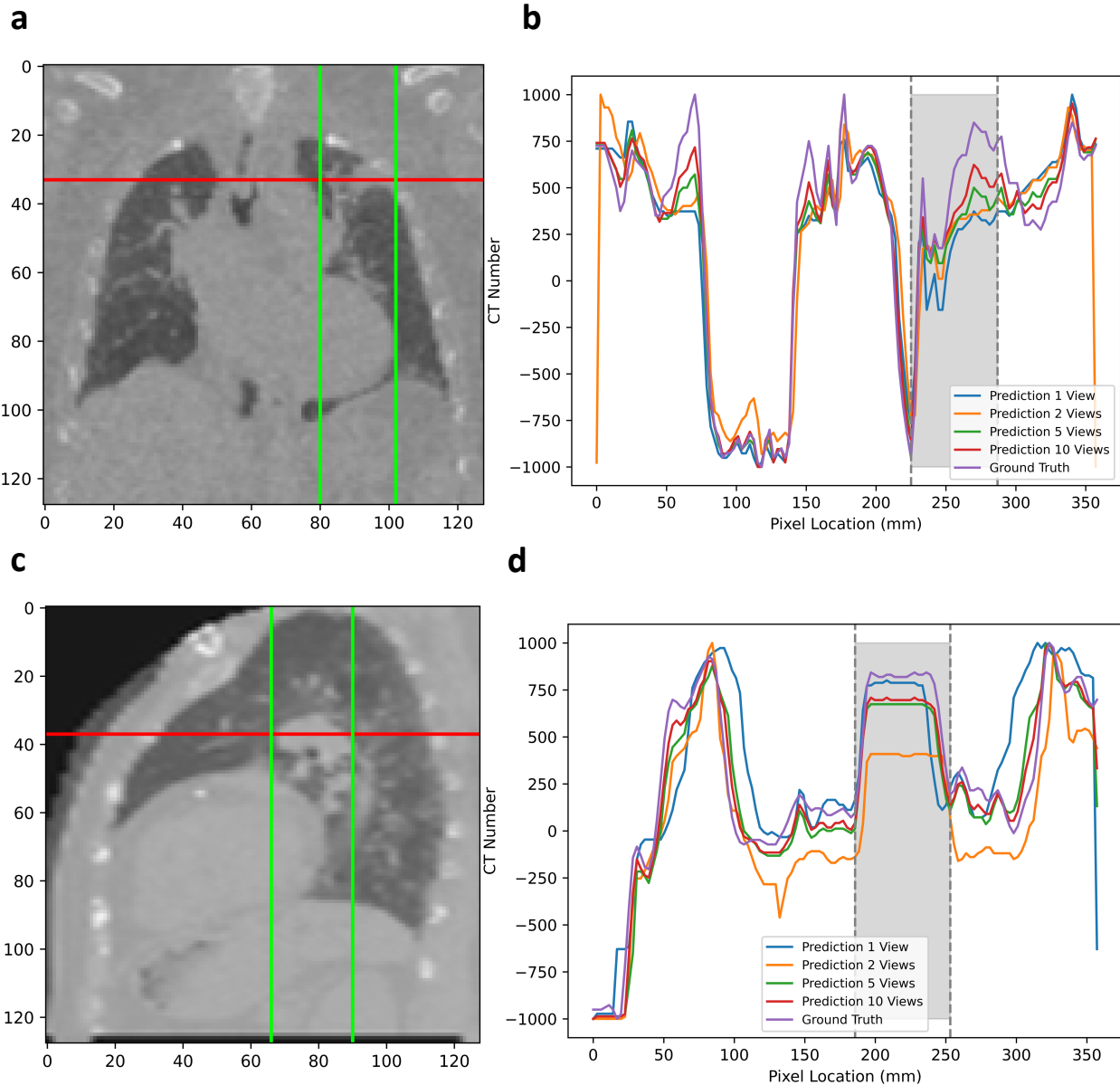

Figure 5. Line profile comparison of the two patients shown in Fig. 3. The images visualized in **a** and **c** are GT slices downsampled to 128×128 to align with the prediction resolution. **a,** Indication of the location of the profile in patient 1 in coronal view across the lung tumor. **b,** Line profiles of 3D images rendered by TomoGRAF with 1, 2, 5, and 10-view inputs for patient 1. **c,** Indication of the location of the profile in patient 2 across the lung tumor in sagittal view. **d,** Line profiles of 3D images rendered by TomoGRAF with 1, 2, 5, and 10-view inputs for patient 2.

Discussion

This paper presents a GAN-embedded NeRF generator (TomoGRAF) for volumetric CT rendering from ultra-sparse X-ray views. TomoGRAF extends radiance fields into medical imaging reconstruction with a CT imaging-informed ray casting/tracing simulator. Also, TomoGRAF leverages the availability of 3D volumetric information at the training stage to enable an effective generator trained with full volumetric supervision. The robustness of TomoGRAF is demonstrated on an external dataset independent of the training set. TomoGRAF vastly improves 1-view 3D reconstruction performance yet scales well with variable views for a wide range of image-guided clinical settings.

Reconstruction of 3D CT volume from ultra-sparse angular sampling is an ill-posed inverse problem that is extremely underconditioned to solve. On the other hand, such 3D reconstruction is practically desirable and widely applicable when a full gantry rotation is prevented by mechanical limitations or the dynamic process of interest is significantly faster than CT acquisition speed[5,6,9]. Therefore, there has been a consistent effort to reconstruct 3D images with extremely sparse views that circumvent these mechanical and temporal restrictions. Although CS-powered iterative methods and some earlier DL methods were able to reconstruct 3D images with as few as 20 views[18], the resultant image quality noticeably degraded. Still, they were unable to meet the challenges of many aforementioned practical scenarios where only one or two views were available for a given anatomical instance. Reconstruction with even more sparse views cannot be achieved without stronger priors and statistical learning. DL methods marched further in realizing ultra-sparse sampling (1 view) reconstruction using state-of-the-art (SOTA) networks, two of which are compared in this study.

TomoGRAF is distinctly superior to two SOTA methods for ultra-sparse view CT reconstruction in the following aspects. 1) In comparison to CNN-based networks with an extremely large number of parameters, such as X2CT-GAN[41], the radiance field-based generators train a lighter model with significantly fewer parameters (X2CT-GAN: ~4.28G FLOPS vs. TomoGRAF ~0.9G FLOPS, FLOPS: floating point operation per second) to represent the interaction process between photons and objects, which formalizes a better-defined goal for the network to reach and can effectively reduce the amount of training data required for achieving global robustness. Plus, CNN frameworks generally lack flexibility in view referencing. The number and angle of views at the inference stage must align with the input at the training stage. Meanwhile, TomoGRAF, besides 1-view referencing, can leverage additional X-ray views at arbitrary angles. It is worth noting that X2CT-GAN performance in the current study is markedly worse than the original report[41]. To determine the correctness of our implementation, we tested the X2CT-GAN code on the LIDC-IDRI data with the same data split and arrived at a similar performance. We believe the sharp decline in performance from internal LIDC-IDRI data testing to external in-house organized data testing is due to the differences in the training and testing data. CT images in LIDC-IDRI are cropped to keep only the thoracic organs, while our in-house test data are intact CT with the complete patient's chest wall, arms, and neck. Such variation or domain shift is common and expected in practice: the patients can vary in size and be set up with different immobilization devices or arm positions. In stark contrast to X2CT-GAN, TomoGRAF is robust to such variation. 2) Compared to MedNeRF, we adapt NeRF with a physically realistic volume rendering mechanism based on the x-ray transportation properties, where photons pass through the body, and the volumetric photon attenuation along the ray path within the body is the focus of reconstruction. In other words, TomoGRAF learns 3D X-ray image formation physics, whereas MedNeRF

assumes visible light transportation physics and is intended for 2D manifold learning of object surfaces. The limitation is evident in both low quantitative imaging metrics and orthogonal cuts of MedNeRF reconstructed patients: there is better retention of outer patient contour than internal anatomical details, which are largely lost in MedNeRF images. Additionally, TomoGRAF employs paired 3D CT supervision at the training stage to maximize the prior knowledge exposed to the network, which contributed to the model robustness in volume rendering at the inference stage. As a result, TomoGRAF successfully leverages the efficient object representation capacity of NeRF while overcoming the intrinsic limitations due to its lack of X-ray transportation physics and 3D volume comprehension. To our knowledge, TomoGRAF is the first truly generalizable single-view 3D X-ray reconstruction pipeline robust to substantial domain shifts.

At the practical level, TomoGRAF provides a unique solution for applications where only one or a few X-ray views are available, but 3D volumetric information is desired. The applications include image-guided radiotherapy, interventional radiology, and angiography. For the former, 2D kV X-rays can be interlaced with MV therapeutic X-ray beams to provide a real-time view of the patient during treatment[54]. However, the 2D projection images do not describe the full 3D anatomy, which is critical for adapting radiotherapy to the real-time patient target and surrounding tissue geometry. Similarly, 4D CT digitally subtracted angiography (DSA) better describes dynamics of the contrast for enhanced diagnosis than single-phase CT DSA[55], but fast helical and flat panel-based 4D-DSA requires repeated scans of the subject, increasing the imaging dose and leading to compromised temporal resolution for intricate vascular structures[56]. TomoGRAF can be potentially used to infer real-time time-resolved 3D DSA with significantly reduced imaging dose. Our results show that TomoGRAF is flexible in incorporating more views for further improved inference performance. Dual views with fixed X-ray systems are widely used in radiotherapy for stereotactic localization[38,57,58], but the modality is limited to triangulating bony anatomies or implanted fiducials. TomoGRAF can utilize the same 2D stereotactic views to provide rich 3D anatomies for soft tissue-based registration and localization. Besides mechanical and imaging dose constraints, inexpensive portable 2D X-rays are more readily available for point-of-care and low-resource settings where a CT is impractical. The ability to reconstruct 3D volumes using a single 2D view would markedly increase the imaging information available for clinical decisions. Our study also shows the feasibility of using more views in TomoGRAF for further improved performance and broader applications, including 4D CBCT and tomosynthesis with sparse or limited angle views.

At the theoretical level, TomoGRAF validates the extremely high data efficiency of neural field representation of 3D voxelized medical images. TomoGRAF, for the first time, materializes high data efficiency, achieving good quality (SSIM=0.79-0.93) 3D reconstruction of CT images with 1-10 views, which is a major stride in comparison to existing research using NeRF or GRAF. The work thus has significant implications in 3D image acquisition, storage, and processing, which are currently voxel-based. Voxelized 3D representation does not provide intrinsic structural information regarding the relationships among voxels and thus can be expensive to acquire and reconstruct. Previous compressed sensing research explored some of the explicit structural correlations, such as piece-wise smoothness, for reduced data requirements. TomoGRAF indicates a new form of data representation that exploits implicit structural information with higher efficiency than conventional methods or neural networks without encoded physics.

Nevertheless, the current study leaves several areas for future improvement. First, TomoGRAF requires further fine-tuning at the inference stage, which increases the reconstruction time (1-view at 344.25±10.32 s and 2-view at 719.46±26.78 s). The time further increases with inference using more views. Significant acceleration is desired for online procedures such as motion adaptive radiotherapy[59]. A larger dataset with a more diverse distribution will eliminate or reduce the burden of the fine-tuning step and bring TomoGRAF inference to a sub-second level, which would be essential for interventional procedures. Second, TomoGRAF is developed and tested on CT-synthesized DRR, which differs from kV X-rays obtained using an actual detector in image characteristics due to simplification of the physical projection model, detector dynamic ranges, noise, pre and postprocessing[39]. The current model may need to be adapted based on actual X-ray projections. Third, TomoGRAF reconstruction results with 1-view are geometrically correct but lose fine details and CT number accuracy, which is partially mitigated with increasing views up to 10. Therefore, in its current form, TomoGRAF is suited for object detection and localization tasks, but its appropriateness for quantitative tasks such as radiation dose calculation needs to be further studied. Moreover, the recovery of detail should also improve with reconstruction resolution, which is currently limited in rendering a maximum of 128 times 128 times 128 resolution due to GPU memory constraints. This limitation, however, is expected to be overcome soon with rapidly-increasing GPU memory capacity.

Conclusion

TomoGRAF, a novel GAN-based NeRF generator, is presented in the current work. TomoGRAF is trained on a public dataset and evaluated on 100 in-house lung CTs. TomoGRAF reconstructed good quality 3D images with correct internal anatomies using 1-2 X-ray views, which state-of-the-art DL methods fail to accomplish. TomoGRAF performance further improves with more views. The superior TomoGRAF performance is attributed to novel x-ray physics encoding in the radiance field training and paired 3D CT supervision.

Materials and Methods

1.1 Problem Formulation

As illustrated in Fig. 1 (d), we formulated the problem of 3D image reconstruction from 2D projection(s) into a GAN-based DL framework, including modules of generator G and discriminator equation, given a series of 2D projections X denoted as $\{X_1, X_2, \cdots, X_N\}$ where $X_i \in \mathbb{R}^2 = \mathbb{R}^{H \times W}$ for $i \in [1, N]$, N is the number of available 2D projections, H and W is the projection height and width. Our modeling target was to form a G that can predict the 3D volume $\hat{Y} \in \mathbb{R}^3 = \mathbb{R}^{D \times H \times W}$ (D represents volume depth) where G is supervised by X and 3D volume GT $Y \in \mathbb{R}^3 = \mathbb{R}^{D \times H \times W}$, and is penalized by D to encourage optimal convergence.

1.2 TomoGRAF Framework

TomoGRAF does not aim to optimize densely posed projections for rendering a single patient volume. Instead, it targets fitting a network for synthesizing new patient volume by learning on various unposed projections. Note that the generator and discriminator work on image patches and sub-volumes during training for better efficiency, whereas a complete patient volume is rendered at inference time. The detailed components in TomoGRAF are shown in Fig. 1 (e, f, g). In what follows, we elaborate on the model architecture.

1.2.1 Generator

Adapted from GRAF[43], Our generator consists of three main components: ray sampling, conditional generative radiance field, and projection rendering. Ray sampling modules render the x-ray paths in 3D that are associated with truth patch/sub-volume, and the conditional generative radiance field module predicts the material density from a 3D location along the rendered x-ray paths. Lastly, the projection rendering module obtains the 2D composition from the predicted volumetric material densities. Overall, the generator G takes x-ray source setup matrix K, view direction (pose) $\xi = (\theta, \phi)$, 2D sampling pattern v and shape, and appearance codes $z_{sh} \in \mathbb{R}^{M_s}$ and $z_a \in \mathbb{R}^{M_a}$ as input, and predicts a size $D \times M \times M$ CT sub-volume $V' \in \mathbb{R}^3 = \mathbb{R}^{D \times M \times M}$ as well as the associated size $M \times M$ CT projection patch $P' \in \mathbb{R}^2 = \mathbb{R}^{M \times M}$ (M is a hyper-parameter defined by user; $M = 32$ is used in our experiments). K consists of $d = (d_1, d_2)$, d_1 is distance of source to patient (SAD), d_2 is distance of source to detector (SID). The detector resolution $S \in \mathbb{R}^2$ and M is bounded by (H, W).

Ray Sampling: The rendered rays $r \in \mathbb{R}^3$ are constrained by ξ, K and P'. The x-ray pose ξ is sampled from a predefined pose distribution p_ξ collected from projection angles in training data with the x-ray source facing towards the origin of the coordinate system all the time. As shown in Fig. 1 (f), $v = (u, s)$ determines the center $u = (x', y') \in \mathbb{R}^2$ and scales $s \in \mathbb{R}^+$ of P' that we target to predict, where V' is formed with all the corresponding 3D coordinates that form P'. At the training stage, u and s are uniformly drawn from $u \sim U(\Omega)$ and $s \sim U[1, S]$ where Ω defined the 2D projection domain and $S = \min(H, W)/M$. Noteworthily, the coordinates in P' and V' are real numbers for the purpose of continuous radiance field evaluation. Following the stratified sampling approach in Mildenhall et al.[45], Q number of points are sampled along each r. The number of rays $R = M \times M$ and R= $H \times W$ per training and inference, respectively.

Conditional Generative Radiance Field: Adapted from GRAF[43], the radiance field is represented by a deep fully connected coordinate network g_ϑ with the input of the positional encoding of a 7D vector $(x, y, z, \theta, \phi, z_{sh}, z_a)$ consisting of 3D location $x = (x, y, z)$ and projection pose ξ. The output is the material density δ in the corresponding x, where ϑ represents the network parameters and $z_{sh} \sim p_{sh}$ and $z_a \sim p_a$ with p_{sh} and p_a drawn from standard Gaussian distribution.

$$g_\vartheta: \mathbb{R}^{\mathcal{L}_x} \times \mathbb{R}^{\mathcal{L}_\xi} \times \mathbb{R}^{M_{sh}} \times \mathbb{R}^{M_a} \to \mathbb{R}^3 \times \mathbb{R}^+ \tag{1}$$
$$(\gamma(x), \gamma(\xi), z_{sh}, z_a) \to \delta \tag{2}$$

Where $\mathcal{L}_x$ and $\mathcal{L}_\xi$ represent the latent codes of x and ξ, M_{sh} and M_a define the shape and appearance codes with $z_{sh} \in \mathbb{R}^{M_{sh}}$ and $z_a \in \mathbb{R}^{M_a}$, and $\gamma(\cdot)$ represents positional encoding.

The architecture of g_ϑ is visualized in Fig. 1 (g) with Equation (3-6). First, shape encoding h_ϑ is conducted with the input of $\gamma(x)$ and z_{sh}. Second, h_ϑ is concatenated with $\gamma(\xi)$ and z_a and then sent to the density head d_ϑ to predict δ.

$$h_\vartheta: \mathbb{R}^{\mathcal{L}_x} \times \mathbb{R}^{M_{sh}} \to \mathbb{R}^H \tag{3}$$
$$(\gamma(x), z_{sh}) \to h \tag{4}$$

$$d_\vartheta: R^H \times \mathbb{R}^{\mathcal{L}\xi} \times \mathbb{R}^{M_a} \to \mathbb{R}^1 \tag{5}$$
$$(\boldsymbol{h}, \gamma(\boldsymbol{\xi}), z_a) \to \delta \tag{6}$$

where the encoding was implemented with a fully connected network with ReLU activation.

Projection Rendering: Lastly, given the material density $\{\delta_i^r\} = V' \in \mathbb{R}^3$ where $1 \le i \le Q$ of all points along the rays $\{r_j\}$ where $1 \le j \le M \times M$ in training, we used a CT projection algorithm[47] to synthetic 2D radiograph patch P' given preset $\boldsymbol{K}$ and $\boldsymbol{\xi}$.

1.2.2 Discriminator
Following the discriminator architecture defined in MedNeRF[42], two self-supervised auto-encoded CNN discriminators,[48] $D_{1,\emptyset}$ and $D_{2,\emptyset}$ compare predicted sub-volume V' to real sub-volume V extracted from real volume Y and predict projection patch P' to real projection patch P extracted from real projection I, respectively. $D_{1,\emptyset}$ is defined to convolve in 3D while $D_{2,\emptyset}$ is defined to convolve in 2D to align with the dimension of its discrimination targets. For extracting V and P, we first extracted P from a real projection I given $\boldsymbol{v}$ and s randomly drawn from their corresponding distributions, and then located the coordinates of V from Y based on $\boldsymbol{\xi}$ and $\boldsymbol{K}$. $D_{1,\emptyset}$ and $D_{2,\emptyset}$ are backpropagated separately with their respective weights, while we defined them to share weights while discriminating different sub-volume/patch locations.

1.2.3 Loss function
Training stage: Our loss objective consists of discrimination towards patch as well as sub-volume predictions. First, the global structures in intermediate decoded patches of $D_{1,\emptyset}$ and $D_{2,\emptyset}$ were separately assessed by Learned Perceptual Image Patch Similarity (LPIPS)[49] (denoted in Equation (7-8)).

$$L_{r,V} = E_{f_v \sim D_1(v), v \sim V}[\frac{1}{whd}\left\|\emptyset_i(\mathcal{G}(\boldsymbol{f_v})) - \emptyset_i(\mathcal{T}(v))\right\|_2] \tag{7}$$

$$L_{r,P} = E_{f_p \sim D_2(p), p \sim P}[\frac{1}{whd}\left\|\emptyset_i(\mathcal{G}(\boldsymbol{f_p})) - \emptyset_i(\mathcal{T}(p))\right\|_2] \tag{8}$$

Where $\emptyset_i(\cdot)$ denotes the output from the ith layer of the pretrained VGG16[50] network, $\boldsymbol{f_v}$ and $\boldsymbol{f_p}$ represent the feature maps from $D_{1,\emptyset}$ and $D_{2,\emptyset}$, w, h and d stands for the width, height and depth of the corresponding feature space, $\mathcal{G}$ is the pre-processing on $\boldsymbol{f}$, and $\mathcal{T}$ is the processing on truth sub-volumes/patches.

Second, hinge loss was selected to classify P' from P and V' from V with formulas listed in Equation (9-10).

$$L_{h,V} = E_{v' \sim V'}[f(D_{1,\emptyset}(v'))] + E_{v \sim V}[f(-D_{1,\emptyset}(v))] \tag{9}$$

$$L_{h,P} = E_{p' \sim P'}[f(D_{2,\emptyset}(p'))] + E_{p \sim P}[f(-D_{2,\emptyset}(p))] \tag{10}$$

Where $f(t) = \max(0, 1 + t)$.

Lastly, data augmentation, including random flipping and rotation, was implemented to V' and P' prior to sending into $D_{1,\emptyset}$ and $D_{2,\emptyset}$, following the theory proposed by Data Augmentation Optimized for GAN (DAG) framework[51]. $D_{1,\emptyset}/D_{2,\emptyset}$ share weights while discriminating multiple

augmented sub-volumes/patches. Therefore, we have the overall loss objective formulated as Equation (11-12).

$$L\left(\vartheta, \{\emptyset_{1,k}\}, \{\emptyset_{2,k}\}\right) = L\left(\vartheta, \emptyset_{1,0}, \emptyset_{2,0}\right) + \frac{\lambda_1}{n-1} \sum_{k=1}^{n} L\left(\vartheta, \emptyset_{1,k}, \emptyset_{2,k}\right) \qquad (11)$$

$$L\left(\vartheta, \emptyset_{1,k}, \emptyset_{2,k}\right) = L_{r,V,k} + L_{h,V,k} + \lambda_2\left(L_{r,P,k} + L_{h,P,k}\right) \qquad (12)$$

Where $n = 4$, $\lambda_1 = 0.2$ and $k = 0$ corresponding to the identity transformation follows the definition in Trans et al[51]. $\lambda_2 = 0.5$ to give the model more attention on conformal V' rendering.

Inference Stage: A fully trained G_ϑ was further fine-tuned with z_{sh} and z_a using the referenced sparse view projection(s) prior to rendering the final volumetric prediction $\hat{Y}$. Since we conducted moderate optimization with limited iterations, G_ϑ was tuned with fully size I instead of patches. Depending on the available views, a referenced projection was randomly drawn for each iteration until G_ϑ reached the convergence criteria. In our experiments, peak signal-to-noise ratio (PSNR)=25 was set as the stopping threshold. The inference loss objective is defined in Equation (13) with a combination of LPIPS, PSNR, and the negative log-likelihood loss (NLL).

$$L_{G_\vartheta} = \lambda_1 L_{r,I} + \lambda_2 L_{PSNR,I} + \lambda_3 L_{NLL,I} \qquad (13)$$

Where $\lambda_1 = \lambda_3 = 0.3$ and $\lambda_2 = 0.1$ were set in our experiments.

1.3 Implementation Details
During training, the RMSprop optimizer[52] with a batch size of 4 (4 × 1), learning rate of 0.0005 for the generator, learning rate of 0.0001 for the discriminator, and 40000 iterations were performed. Per inference fine-tuning, RMSprop[52] optimizer with a batch size of 1, learning rate of 0.0005, stopping threshold of PNSR=25 (mostly under 1000 iterations) was implemented towards the generator. All the experiments were carried out on a NVDIA RTX 4×A6000 cluster.

1.4 Evaluation Metrics
We evaluate the predicted CT volume $\hat{Y}$ and projection $\hat{I}$ corresponding to the reference view of our TomoGRAF generator using PSNR, structure similarity index measurement (SSIM) and rooted mean squared error (RMSE) as Equation (14-16).

$$PSNR = 20 \cdot \log_{10} \frac{MAX_I}{RMSE}$$

(14)

$$SSIM = \frac{(2\mu_{G_\vartheta}\mu_y + c_1)(2\sigma_{G_\vartheta y} + c_2)}{(\mu_{G_\vartheta}^2 + \mu_y^2 + c_1)(\sigma_{G_\vartheta}^2 + \sigma_y^2 + c_2)}$$

(15)

$$SSIM = \sqrt{\frac{\sum_{i=1}^{N} ||y(i) - \hat{y}(i)||^2}{N}}$$

(16)

Where MAX_I is the max possible pixel value in a tensor, RMSE stands for rooted mean squared error, μ_{G_ϑ} and μ_y is the pixel mean of G_ϑ and y and $\sigma_{G_\vartheta y}$ is the covariance between G_ϑ and y, $\sigma_{G_\vartheta}^2$

and σ_y^2 is the variance of G_ϑ and y. Lastly, $c_1 = (k_1 L)^2$ and $c_2 = (k_2 L)^2$, where $k_1 = 0.01$ and $k_2 = 0.03$ in the current work and L is the dynamic range of the pixel values $(2^{\# \, bits \, per \, pixel} - 1)$.

1.5 Baseline Algorithms

A CNN-based method X2CT-GAN[41], and a NeRF-based method MedNeRF [42] were included as our benchmarks with both the performance in projection inference and CT volume rendering compared. X2CT-GAN and MedNeRF are evaluated using the open-sourced codes and network weights released by authors, with the input of our in-house test set arranged following their data organization guidelines.

1.6 Data Cohorts

1011 CT scans were selected from LIDC-IDRI[53] thoracic CT database for organizing the training set. Digital reconstructed radiographs (DRRs) were generated as projections for training supervision. Several scanner manufacturers and models were included (GE Medical Systems LightSpeed scanner models, Philips Brilliance scanner models, Siemens Definition, Siemens Emotion, Siemens Sensation, and Toshiba Aquilion). The tube peak potential energies for scan acquisition include 120 kV, 130 kV, 135 kV, and 140 kV. The tube current is in the range of 40-627 mA. Slice thickness includes 0.6 mm, 0.75 mm, 0.9mm, 1.0 mm, 1.25 mm, 1.5 mm, 2.0 mm, 2.5 mm, 3.0 mm, 4.0 mm and 5.0 mm. The in-plane pixel size ranges from 0.461 to 0.977 mm[53]. 72 DRRs that cover a full 360° (generated each of 5° rotations) vertical rotations were generated for each scan. All the DRRs and CT volumes were black-border cropped out. DRRs were resized with a resolution of 128 times 128, and CT volumes were interpolated with a resolution of $128 \times 128 \times 128$ for model learning preparation. All the data were normalized to [0, 1].

The test data was organized under IRB approval (IRB # 20-32527) and included 100 de-identified CT scans from lung cancer patients who underwent robotic radiation therapy. All patients were scanned by Siemens Sensation with tube peak potential energy of 120 kV, tube current of 120 mA, slice thickness of 1.5 mm, and in-plane pixel size of 0.977 mm. The anterior-posterior (AP) and lateral views were generated for inference reference, with 1-view-based inference solely referencing the AP view projection. All the DRRs and CT volumes had the black border cropped out. Additionally, DRRs were resized with a resolution of 128×128, and CT volumes were interpolated with a volume size of $128 \times 128 \times 128$. All the data were normalized to [0, 1] prior to being fed into models for inference.

1.7 Model performance as a function of the number of views and 3D supervision

The model baseline performance was established using a single AP view. 1, 2, 5, and 10 view reconstructions were also performed to determine the model performance. The view angles are specified as follows: for 1-view-based reconstruction, the AP view is used for referencing. For 2-view-based reconstruction, the AP and lateral views are used for inferencing. For 5-view-based reconstruction, a full 360° is covered with rotation every 72°, starting from the AP view. For 10-view-based reconstruction, a full 360° is covered with rotation of every 36°, starting from the AP view.

Code and data share

The source code of TomoGRAF will be publicly shared upon paper publication. TomoGRAF was trained using a public patient CT database LIDC-IDRI (https://wiki.cancerimagingarchive.net/pages/viewpage.action?pageId=1966254). The private patient dataset for testing will be shared via NCI TCIA as well.

References

1.   Tuy, H. K. An Inversion Formula for Cone-Beam Reconstruction. *SIAM J. Appl. Math.* **43**, 546–552 (1983).

2.   Ma, C.-M. C. & Paskalev, K. In-room CT techniques for image-guided radiation therapy. *Medical Dosimetry* **31**, 30–39 (2006).

3.   Gupta, R. *et al.* CT-Guided Interventions: Current Practice and Future Directions. in *Intraoperative Imaging and Image-Guided Therapy* (ed. Jolesz, F. A.) 173–191 (Springer New York, New York, NY, 2014). doi:10.1007/978-1-4614-7657-3_12.

4.   Eschrich, S. A. *et al.* Validation of a Radiosensitivity Molecular Signature in Breast Cancer. *Clinical Cancer Research* **18**, 5134–5143 (2012).

5.   Vedantham, S., Karellas, A., Vijayaraghavan, G. R. & Kopans, D. B. Digital Breast Tomosynthesis: State of the Art. *Radiology* **277**, 663–684 (2015).

6.   Sechopoulos, I. A review of breast tomosynthesis. Part II. Image reconstruction, processing and analysis, and advanced applications. *Medical Physics* **40**, 014302 (2013).

7.   Kim, K. *et al.* Sparse-view spectral CT reconstruction using spectral patch-based low-rank penalty. *IEEE Trans Med Imaging* **34**, 748–760 (2015).

8.   Rui, X. *et al.* Ultra-low dose CT attenuation correction for PET/CT: analysis of sparse view data acquisition and reconstruction algorithms. *Phys Med Biol* **60**, 7437–7460 (2015).

9.   Meinel, F. G. *et al.* Time-resolved CT angiography in aortic dissection. *European Journal of Radiology* **81**, 3254–3261 (2012).

10.   Shieh, C., Kipritidis, J., O'Brien, R. T., Kuncic, Z. & Keall, P. J. Image quality in thoracic 4D cone-beam CT: A sensitivity analysis of respiratory signal, binning method, reconstruction algorithm, and projection angular spacing. *Medical Physics* **41**, 041912 (2014).

11.   Feldkamp, L. A., Davis, L. C. & Kress, J. W. Practical cone-beam algorithm. *J. Opt. Soc. Am. A* **1**, 612 (1984).

12.   Gordon, R., Bender, R. & Herman, G. T. Algebraic Reconstruction Techniques (ART) for three-dimensional electron microscopy and X-ray photography. *Journal of Theoretical Biology* **29**, 471–481 (1970).

13.   Andersen, A. H. & Kak, A. C. Simultaneous Algebraic Reconstruction Technique (SART): A Superior Implementation of the Art Algorithm. *Ultrason Imaging* **6**, 81–94 (1984).

14.   Donoho, D. L. Compressed sensing. *IEEE Trans. Inform. Theory* **52**, 1289–1306 (2006).

15.   Sidky, E. Y. & Pan, X. Image reconstruction in circular cone-beam computed tomography by constrained, total-variation minimization. *Phys Med Biol* **53**, 4777–4807 (2008).

16.   Liu, Y., Ma, J., Fan, Y. & Liang, Z. Adaptive-weighted total variation minimization for sparse data toward low-dose x-ray computed tomography image reconstruction. *Phys Med Biol* **57**, 7923–7956 (2012).

17.   Liu, Y. *et al.* Total variation-stokes strategy for sparse-view X-ray CT image reconstruction. *IEEE Trans Med Imaging* **33**, 749–763 (2014).

18.   Chen, G.-H., Tang, J. & Leng, S. Prior image constrained compressed sensing (PICCS). in (eds. Oraevsky, A. A. & Wang, L. V.) 685618 (San Jose, CA, 2008). doi:10.1117/12.770532.

19.   Lu, K., He, N. & Li, L. Nonlocal Means-Based Denoising for Medical Images. *Computational and Mathematical Methods in Medicine* **2012**, 1–7 (2012).

20.   Chen, Y. *et al.* Artifact suppressed dictionary learning for low-dose CT image processing. *IEEE Trans Med Imaging* **33**, 2271–2292 (2014).

21.   Chen, Y. *et al.* Thoracic low-dose CT image processing using an artifact suppressed large-scale nonlocal means. *Phys. Med. Biol.* **57**, 2667–2688 (2012).

22.   Burger, H. C., Schuler, C. J. & Harmeling, S. Image denoising: Can plain neural networks compete with BM3D? in *2012 IEEE Conference on Computer Vision and Pattern Recognition* 2392–2399 (IEEE, Providence, RI, 2012). doi:10.1109/CVPR.2012.6247952.

23.   Burger, H. C., Schuler, C. J. & Harmeling, S. Image denoising with multi-layer perceptrons, part 1: comparison with existing algorithms and with bounds. Preprint at http://arxiv.org/abs/1211.1544 (2012).

24.   Prakash, P. *et al.* Reducing Abdominal CT Radiation Dose With Adaptive Statistical Iterative Reconstruction Technique: *Investigative Radiology* **45**, 202–210 (2010).

25.   Kang, E., Min, J. & Ye, J. C. A deep convolutional neural network using directional wavelets for low-dose X-ray CT reconstruction. *Med Phys* **44**, e360–e375 (2017).

26.   Kyong Hwan Jin, null, McCann, M. T., Froustey, E. & Unser, M. Deep Convolutional Neural Network for Inverse Problems in Imaging. *IEEE Trans Image Process* **26**, 4509–4522 (2017).

27.   Pelt, D. M. & Batenburg, K. J. Improving filtered backprojection reconstruction by data-dependent filtering. *IEEE Trans Image Process* **23**, 4750–4762 (2014).

28.   Würfl, T., Ghesu, F. C., Christlein, V. & Maier, A. Deep Learning Computed Tomography. in *Medical Image Computing and Computer-Assisted Intervention - MICCAI 2016* (eds. Ourselin, S., Joskowicz, L., Sabuncu, M. R., Unal, G. & Wells, W.) vol. 9902 432–440 (Springer International Publishing, Cham, 2016).

29.   Ma, X. F., Fukuhara, M. & Takeda, T. Neural network CT image reconstruction method for small amount of projection data. *Nuclear Instruments and Methods in Physics Research Section A: Accelerators, Spectrometers, Detectors and Associated Equipment* **449**, 366–377 (2000).

30.   Li, S. *et al.* Dictionary learning based sinogram inpainting for CT sparse reconstruction. *Optik* **125**, 2862–2867 (2014).

31.   Chen, Y. *et al.* Structure-Adaptive Fuzzy Estimation for Random-Valued Impulse Noise Suppression. *IEEE Trans. Circuits Syst. Video Technol.* **28**, 414–427 (2018).

32.   Liu, J. *et al.* Discriminative Feature Representation to Improve Projection Data Inconsistency for Low Dose CT Imaging. *IEEE Trans Med Imaging* **36**, 2499–2509 (2017).

33.   Lee, H., Lee, J. & Cho, S. View-interpolation of sparsely sampled sinogram using convolutional neural network. in (eds. Styner, M. A. & Angelini, E. D.) 1013328 (Orlando, Florida, United States, 2017). doi:10.1117/12.2254244.

34.   Podgorsak, A. R., Shiraz Bhurwani, M. M. & Ionita, C. N. CT artifact correction for sparse and truncated projection data using generative adversarial networks. *Med Phys* **48**, 615–626 (2021).

35.   Sun, J., Li, H. & Xu, Z. Deep ADMM-Net for compressive sensing MRI. *Advances in neural information processing systems* **29**, (2016).

36.   Xu, Y. *et al.* A method for volumetric imaging in radiotherapy using single x-ray projection. *Med Phys* **42**, 2498–2509 (2015).

37.   Hrinivich, W. T. *et al.* Effect of subject motion and gantry rotation speed on image quality and dose delivery in CT-guided radiotherapy. *Medical Physics* **49**, 6840–6855 (2022).

38.   Xu, D. *et al.* Deep match: A zero-shot framework for improved fiducial-free respiratory motion tracking. *Radiotherapy and Oncology* 110179 (2024) doi:10.1016/j.radonc.2024.110179.

39.   Schafer, S. & Siewerdsen, J. H. Technology and applications in interventional imaging: 2D X-ray radiography/fluoroscopy and 3D cone-beam CT. in *Handbook of Medical Image Computing and Computer Assisted Intervention* 625–671 (Elsevier, 2020). doi:10.1016/B978-0-12-816176-0.00031-4.

40.   Shen, L., Zhao, W. & Xing, L. Patient-specific reconstruction of volumetric computed tomography images from a single projection view via deep learning. *Nat Biomed Eng* **3**, 880–888 (2019).

41.   Ying, X. *et al.* X2CT-GAN: Reconstructing CT from Biplanar X-Rays with Generative Adversarial Networks. Preprint at http://arxiv.org/abs/1905.06902 (2019).

42.   Corona-Figueroa, A. *et al.* MedNeRF: Medical Neural Radiance Fields for Reconstructing 3D-aware CT-Projections from a Single X-ray. in *2022 44th Annual International Conference of the IEEE Engineering in Medicine & Biology Society (EMBC)* 3843–3848 (IEEE, Glasgow, Scotland, United Kingdom, 2022). doi:10.1109/EMBC48229.2022.9871757.

43.   Schwarz, K., Liao, Y., Niemeyer, M. & Geiger, A. GRAF: Generative Radiance Fields for 3D-Aware Image Synthesis. Preprint at http://arxiv.org/abs/2007.02442 (2021).

44.   Shen, D., Wu, G. & Suk, H.-I. Deep Learning in Medical Image Analysis. *Annu. Rev. Biomed. Eng.* **19**, 221–248 (2017).

45.   Mildenhall, B. *et al.* NeRF: Representing Scenes as Neural Radiance Fields for View Synthesis. Preprint at http://arxiv.org/abs/2003.08934 (2020).

46.   Isola, P., Zhu, J.-Y., Zhou, T. & Efros, A. A. Image-to-Image Translation with Conditional Adversarial Networks. (2016) doi:10.48550/ARXIV.1611.07004.

47.   Sherouse, G. W., Novins, K. & Chaney, E. L. Computation of digitally reconstructed radiographs for use in radiotherapy treatment design. *International Journal of Radiation Oncology*Biology*Physics* **18**, 651–658 (1990).

48.   Liu, B., Zhu, Y., Song, K. & Elgammal, A. Towards Faster and Stabilized GAN Training for High-fidelity Few-shot Image Synthesis. Preprint at http://arxiv.org/abs/2101.04775 (2021).

49.   Zhang, R., Isola, P., Efros, A. A., Shechtman, E. & Wang, O. The Unreasonable Effectiveness of Deep Features as a Perceptual Metric. Preprint at http://arxiv.org/abs/1801.03924 (2018).

50.   Simonyan, K. & Zisserman, A. Very Deep Convolutional Networks for Large-Scale Image Recognition. *arXiv:1409.1556 [cs]* (2015).

51.   Tran, N.-T., Tran, V.-H., Nguyen, N.-B., Nguyen, T.-K. & Cheung, N.-M. On Data Augmentation for GAN Training. *IEEE Trans. on Image Process.* **30**, 1882–1897 (2021).

52.   Kingma, D. P. & Welling, M. Auto-Encoding Variational Bayes. Preprint at http://arxiv.org/abs/1312.6114 (2022).

53.   Armato, S. G. *et al.* The Lung Image Database Consortium (LIDC) and Image Database Resource Initiative (IDRI): A Completed Reference Database of Lung Nodules on CT Scans. *Medical Physics* **38**, 915–931 (2011).

54.   Li, R. *et al.* Intrafraction verification of gated RapidArc by using beam-level kilovoltage X-ray images. *Int J Radiat Oncol Biol Phys* **83**, e709-715 (2012).

55.   Haubenreisser, H. *et al.* From 3D to 4D: Integration of temporal information into CT angiography studies. *Eur J Radiol* **84**, 2421–2424 (2015).

56.   Keil, F. *et al.* 4D Flat Panel Conebeam CTA for Analysis of the Angioarchitecture of Cerebral AVMs with a Novel Software Prototype. *AJNR Am J Neuroradiol* **43**, 102–109 (2022).

57.   Lewis, B. C., Snyder, W. J., Kim, S. & Kim, T. Monitoring frequency of intra-fraction patient motion using the ExacTrac system for LINAC-based SRS treatments. *J Appl Clin Med Phys* **19**, 58–63 (2018).

58.   Kilby, W., Dooley, J. R., Kuduvalli, G., Sayeh, S. & Maurer, C. R. The CyberKnife Robotic Radiosurgery System in 2010. *Technol Cancer Res Treat* **9**, 433–452 (2010).

59.   Keall, P. J. *et al.* AAPM Task Group 264: The safe clinical implementation of MLC tracking in radiotherapy. *Medical Physics* **48**, (2021).